Vol 17 No 3, March 2008
1674-1056/2008/17(03)/1041-09

Chinese Physics B

© 2008 Chin. Phys. Soc.
and IOP Publishing Ltd

Three-dimensional lattice Boltzmann method for simulating blood flow in aortic arch*

Kang Xiu-Ying(康秀英)[a)†], Ji Yu-Pin(吉驭嫔)[a)],
Liu Da-He(刘大禾)[a)], and Jin Yong-Juan(金永娟)[b)]

[a)] *Applied Optics Beijing Area Major Laboratory, Department of Physics, Beijing Normal University, Beijing* 100875, *China*
[b)] *Institute of Hematology, Chinese Academy of Medical Sciences, Tianjin* 300020, *China*

(Received 11 December 2006; revised manuscript received 14 September 2007)

The three-dimensional (3D) lattice Boltzmann models, 3DQ15, 3DQ19 and 3DQ27, under different wall boundary conditions and lattice resolutions have been investigated by simulating Poiseuille flow in a circular cylinder for a wide range of Reynolds numbers. The 3DQ19 model with improved Fillippova and Hanel (FH) curved boundary condition represents a good compromise between computational efficiency and reliability. Blood flow in an aortic arch is then simulated as a typical haemodynamic application. Axial and secondary fluid velocity and effective wall shear stress profiles in a 180° bend are obtained, and the results also demonstrate that the lattice Boltzmann method is suitable for simulating the flow in 3D large-curved vessels.

Keywords: lattice Boltzmann method, aortic arch, secondary flow, wall shear stress
PACC: 4730, 4715

1. Introduction

Blood flow, especially its characteristics near bifurcations or curvature of the arteries, is an important topic in the study of hemodynamics. There is a number of evidence that suggests a correlation between atherosclerosis and regions with low blood velocity, rotational flow or special shear stress near the walls of the arteries.[1,2] However, this kind of relation is still not fully understood, but is currently receiving more and more attention.

Detailed analysis of the developing fluid flow in bends of vessels was strongly facilitated by improved numerical simulations and in vivo experimental methods for the understanding of blood flow in human arterial system.[3−5] The studies provide excellent insight on the nature of the secondary flow and the resulting skewing of the axial velocity profiles, though the nature of the flow developed in the real human aorta is even more complicated, where the pulsatile flow is extremely complex and unsteady. For simplicity, the propagation of the flow is usually considered as steady flows of different Reynolds numbers. And in many cases numerical simulation is used because in vivo experiments are extremely difficult.

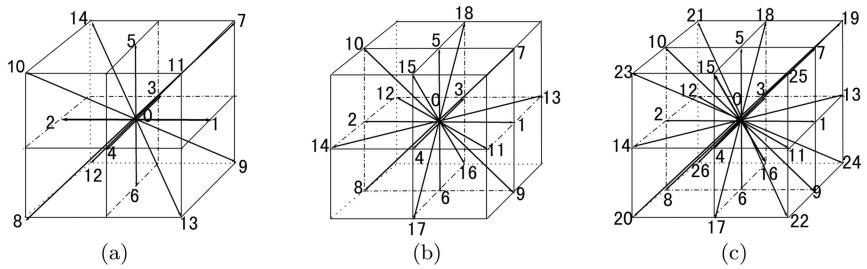
The lattice Boltzmann method[6−10] has recently been proven to be competitive in studying fluid flows in various physical systems. Due to its simple implementation, straightforward parallelization, and easy grid generation, it might be considered a more suitable approach of blood flow simulations.[11−14]

This paper is organized as follows. In Section 2 we briefly describe the 3D lattice Boltzmann method and the boundary conditions. Section 3 is devoted to a detailed comparison among three regularly used 3D models under different boundary conditions. In Section 4, we present our simulation results of flow in aortic arch. Conclusions are presented in Section 5.

2. The 3D lattice Boltzmann method

Lattice Boltzmann method, described by Bhatnagar, Gross and Krook (BGK) who simplified the collision operator, is practically a discretization of a discrete Boltzmann equation of velocity that describes the evolution of particles in kinetic theory. Figure 1 shows the various usually used 3D models such as the D3Q15, the D3Q19 and the D3Q27 models (here D denotes the dimensionality of the problem and Q is the number of bonds per lattice point).

*Project supported by the National Natural Science Foundation of China (Grant No 10274006), and Education Ministry of China (Grant No 03011).
†Corresponding author. E-mail: kangxy@bnu.edu.cn



(a) (b) (c)

Fig.1. The 3D lattice models. (a) 3DQ15; (b) 3DQ19; (c) 3DQ27.

Let $f_i(\boldsymbol{r},t)$ be a non-negative real number describing the distribution function of the fluid density at node $\boldsymbol{r}$ and time t in which the fluid moves in direction $\boldsymbol{e}_i$. The distribution function evolves the single relaxation time BGK operator according to the Boltzmann equation that is discrete in space–time,

$$f_i(\boldsymbol{r}+\boldsymbol{e}_i\cdot\delta t, t+\delta t) = f_i(\boldsymbol{r},t) + \frac{f_i^{\rm eq}-f_i(\boldsymbol{r},t)}{\tau}. \quad (1)$$

Define macroscopic density ρ and velocity $\boldsymbol{u}$ as $\rho = \sum f_i$, $\rho\boldsymbol{u} = \sum f_i\boldsymbol{e}_i$. In Eq.(1) δt is the time step, τ is the relaxation coefficient; $f_i^{\rm eq}$ is the equilibrium distribution function in direction i, which is related to density ρ and velocity $\boldsymbol{u} = (u_x, u_y, u_z)$. A common choice is

$$f_i^{\rm eq} = \rho\omega_i\left[1+\frac{3\boldsymbol{e}_i\cdot\boldsymbol{u}}{c^2}+\frac{9}{2}\frac{(\boldsymbol{e}_i\cdot\boldsymbol{u})^2}{c^4}-\frac{3}{2}\frac{\boldsymbol{u}^2}{c^2}\right], \quad (2)$$

where ω_i is the weight factor depending on the length of the vector $\boldsymbol{e}_i$, and $\boldsymbol{e} = \delta\boldsymbol{x}/\delta t$, with $\delta\boldsymbol{x} = \boldsymbol{e}\delta t$ being the lattice constant. Table 1 lists the weight factors used in the different models.

Table 1. The coefficients ω_i in the equilibrium distribution function $f_i^{\rm eq}$ for the different lattice Boltzmann models.

model	0	I	II	III
3DQ15	2/9	1/9	0	1/72
3DQ19	1/3	1/18	1/36	0
3DQ27	8/27	2/27	1/54	1/216

Note. A 0 indicates a rest particle, I is for links pointing to the nearest neighbours, II is for links pointing to the next-nearest neighbours, III is for links pointing to the next-next-nearest neighbours.

The lattice Boltzmann models presented here yield the correct hydrodynamic behaviour for an incompressible fluid in the limit of low Mach and Knudsen numbers. The macroscopic continuity equation and the Navier–Stokes equation can be obtained by Taylor expansion of the lattice Boltzmann equation up to $o(\delta t^2)$ together with application of a multi-scale Chapman–Enskog procedure,

$$\partial_t\rho + \partial_\alpha(\rho u_\alpha) = 0, \quad (3)$$

$$\partial_t(\rho u_\alpha) + \partial_\beta(\rho u_\alpha u_\beta) = \partial_\alpha p + \nu\partial_\beta[\rho(\partial_\alpha u_\beta + \partial_\beta u_\alpha)], \quad (4)$$

where p and ν are the pressure and viscosity defined by

$$p = c_{\rm s}^2\rho, \quad (5)$$

$$\nu = \frac{(2\tau-1)}{6}c^2\delta t, \quad (6)$$

$c_{\rm s}$ being the sound speed and $c_{\rm s}^2 = c^2/3$.

The stress tensor[15] can be obtained from the non-equilibrium parts of the distribution function,

$$\tau_{\alpha\beta} = -\rho c_{\rm s}^2\delta_{\alpha\beta} - \left(1-\frac{1}{2\tau}\right)\sum_{i=0}(f_i - f_i^{\rm eq})\boldsymbol{e}_{i\alpha}\cdot\boldsymbol{e}_{i\beta}, \quad (7)$$

which gives α- and β- components of the stress tensor.

The effect of the boundary conditions is very important in many fluid dynamical simulations. In lattice Boltzmann method, the bounce-back boundary rule is the simplest and computationally efficient way to impose solid walls. However, it can attain second-order accuracy only if the boundary is fictitiously placed halfway between two nodes. Fillippova and Hanel (abbreviated as FH) curved boundary condition using the interpolation technique can achieve the second-order accuracy in the simulation of a flow with a curved boundary.[16] But when the relaxation coefficient τ is near unity, it induces the computational instability. Afterwards, Mei *et al*[17] improved the stability of the scheme. Due to its better computational accuracy and robustness in handling curved walls, the boundary treatment usually is used to deal with the complex geometry problem.

3. Comparisons among the 3D lattice Boltzmann models under different boundary conditions by simulating a Poiseuille flow in a circular cylinder

In this work, the problem of Poiseuille flow with z axis along the channel direction is used as a benchmark. In this case the analytical solution for the velocity profile is known. The computational accuracy of the 3DQ15, 3DQ19 and 3DQ27 lattice Boltzmann models is investigated under different Reynolds number, boundary conditions, distribution of boundary nodes and number of nodes. Figure 2 shows the 2D projection of the discretized domain and the boundary nodes (denoted by solid symbols) on the xy plane for the flow inside a circular cylinder with a radius $R = 14.0$ lattice units.

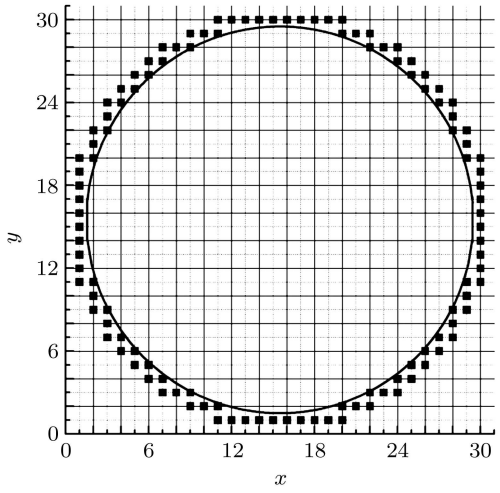


Fig.2. The 2D projection of the discretized domain and boundary nodes.

The relative error between the simulated and theoretical exact solutions was given by

$$\varepsilon = \frac{\left\{\sum\limits_{(x_i,y_j)\in\Omega}[u_{\mathrm{LBM}}(x_i,y_j)-u_{\mathrm{exact}}(x_i,y_j)]^2\right\}^{1/2}}{\left[\sum\limits_{(x_i,y_j)\in\Omega}u^2_{\mathrm{exact}}(x_i,y_j)\right]^{1/2}}, \tag{8}$$

where Ω is the set of the discrete lattice grids inside the pipe cross section, $u_{\mathrm{LBM}}(x_i, y_j)$ and $u_{\mathrm{exact}}(x_i, y_j)$ are the simulated and exact axial velocity functions of the tube, respectively.

3.1. Simulating accuracy of the 3DQ15 and 3DQ19 models under different boundary conditions

The 3DQ15 and 3DQ19 lattice Boltzmann models are usually used in simulations of 3D flow in a cylindrical pipe because they have higher computational effect than the 3DQ27 model has. In the following, test will be made for their simulation errors under three different boundary conditions, i.e, the bounce-back boundary condition, Filippva and Hanel curved boundary condition and its improved boundary condition.

Simulations are first performed by using the 3DQ15 model under the bounce-back condition, the FH curved boundary and its improved boundary condition, separately, with different Reynolds numbers. The pipe radius R is set at 5.0 lattice units and the length is 20. At the inlet and outlet of the tube, the predetermined values of density are imposed on and the common pressure boundary conditions are used.[18] The pipe wall is not slippery. By changing the relaxation coefficient τ, the flow distributions in the pipe are simulated for different Reynolds values. The dependence of the relative error on the Reynolds number and wall boundary conditions is shown in Fig.3.

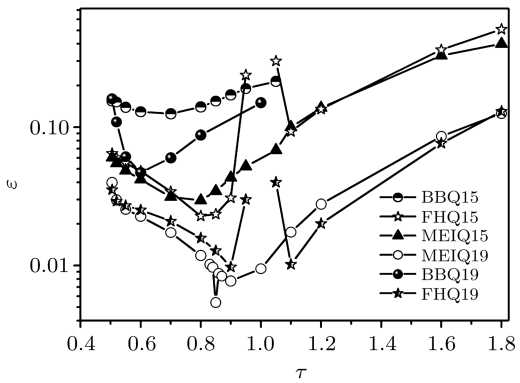


Fig.3. Relative error under different boundary conditions and relaxation coefficient τ using 3DQ15 and 3DQ19 models. (Q15 is for the 3DQ15 and Q19 is for 3DQ19 model, BB for bounce-back boundary, FH for FH curved boundary, and MEI for its improved one).

Similar simulations are performed using the 3DQ19 scheme and the simulated results are shown

in Fig.3. for comparison. The results show that with the decrease of Re, that is, the increase of τ, the error first decreases and subsequently increases after certain optimal value of the relaxation parameter under all the three kinds of boundary conditions. The curved boundary conditions can give better results than the bounce-back condition in dealing with the flows of the complex boundary walls. The modified FH boundary condition can improve the computational stability and accuracy when the relaxation parameter τ is close to unity. But the bounce-back boundary condition has much higher computational efficiency and system stability. In fact, if the simulating error is met, the bounce-back condition is considered a better method for simple geometries. On the other hand, the 3DQ19 model is obviously superior to the 3DQ15 model in accuracy and stability. Although the 3DQ15 model requires 21% less CPU time and storage than the 3DQ19 model does, it is not as robust as the 19-bit model and may actually requires more CPU time and memory to obtain a reasonable solution since more nodes are needed.

3.2. Dependence of computational error on the lattice resolution when using the 3DQ15, 3DQ19 and 3DQ27 models

To test the dependence of computational error on the lattice resolution in 3DQ15, 3DQ19 and 3DQ27 models, the radius of the 3D cylinder is set at $R =$ 5.0, 10.0, 15.0, 20.0, 25.0, 30.0, 40.0, here, R denotes the cylinder radius, and the length of cylinder is enlarged accordingly while the Reynolds number of the flow is always set at a certain fixed value by changing the predetermined density at the tube inlet. In all the simulations, the improved FH curved boundary condition is adopted.

Figure 4 shows the relative errors ε as a function of lattice spacing N_x for the three different 3D lattice Boltzmann models. As demonstrated by Mei *et al*,[17] the total error (including both the flow field and the boundary condition errors) of the simulation decays quadratically. Moreover, the 3DQ19 lattice Boltzmann model is better than the 3DQ15 and 3DQ27 models in accuracy and computational and memory requirements. Thus, it represents a good compromise of both computational efficient and reliability.

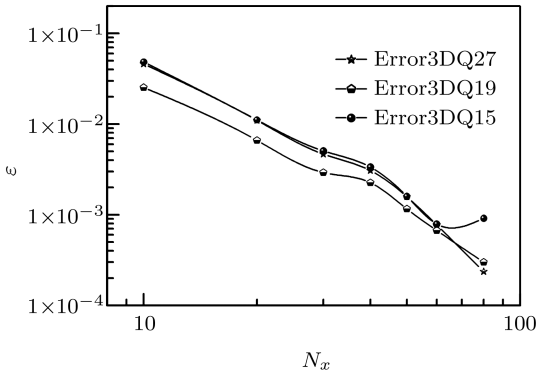


Fig.4. Relative error ε as a function of lattice spacing N_x and cylinder radius for the three different 3D LBM models, $R = 5.0$, 10.0, 15.0, 20.0, 25.0, 30.0, and 40.0 respectively, here, R denotes the cylinder radius.

3.3. Dependence of computational error on the distribution of boundary relative to the local for the 3DQ19 model

Finally, we investigate the dependence of simulation error on the distribution of boundary relative to lattices using the 3DQ19 model under the three boundary conditions stated above. The simulations performed only change the place of the centre of the circular cross-section relative to the local lattice every time, that is, the centre of the circle moves to the corner of the local lattice along its diagonal, and the offset equals $\alpha = 0.1$, 0.2, 0.3, 0.4, and 0.5 respectively.

As seen in Fig.5, computational error varies with the cylinder boundary relative to the local lattices,

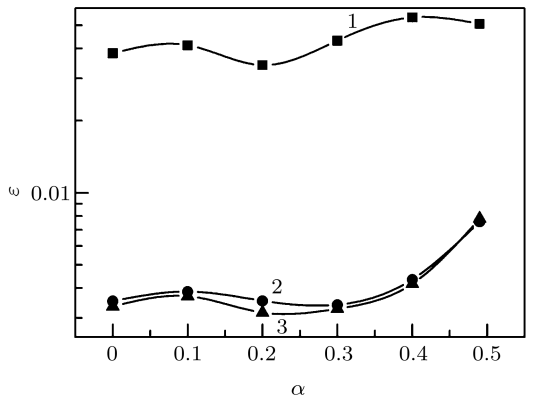


Fig.5. Simulation error by 3DQ19 model for different boundary places relative to the local lattices under the three boundary conditions (1 is for the bounce-back, 2 is the FH, and 3 is improved FH boundary condition).

but the difference of the errors is limited within the same order of accuracy. Furthermore, the simulating

accuracy of the curved boundary conditions is an order of magnitude higher than that obtained using the bounce-back.

4. Simulation of blood flow in aortic arch by lattice Boltzmann method with improved FH curved boundary condition for 3DQ19

4.1. Arch model

The studies on the flow development in curved tubes have gained an insight of the nature of the secondary flow and the resulting skewing of the axial velocity profiles in aortic arch, though the nature of flow development in the human aorta is further complicated by the noncircular cross-section, the secondary and tertiary curvature, tapering, distensibility of the wall, and the branch vessels emanating from the mid-arch region.

Here a 3D arterial arch is considered, which is represented by a curved tube with constant radius $R = 2\,\mathrm{mm}$ and bend radius $R_c = 6\,\mathrm{mm}$. Figure 6 shows the 2D projection of the discretized domain and the boundary nodes (denoted by dots) on the symmetric yz plane of the arch. Blood is regarded as homogeneous and Newtonian fluid because the scale of the

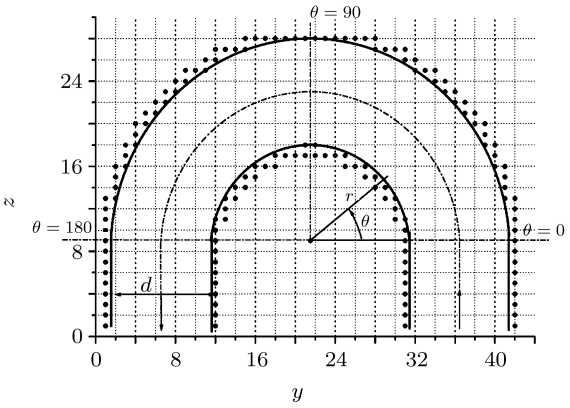


Fig.6. The symmetric yz projection of the discretized domain and the boundary nodes (denoted by dots) of the 3D aortic arch.

suspended microstructure is much smaller than that of the flow in arterial vessels though it is well known that blood is a suspension. The density and kinematic viscosity of the blood flow are taken to be $\rho = 1.05\,\mathrm{g/cm^3}$, $\nu = 0.0381\,\mathrm{cm^2/s}$, respectively. By changing the relaxation coefficient τ, a lot of steady laminar flow simulation is carried out with Reynolds number ($\mathrm{Re} = 2Ru/\nu$, where u is the average velocity in the whole tube) varying from 200 to 1000. At the inlet and outlet of the tube, the FH curved boundary conditions are used, and the velocity of the inlet and outlet is specified by their predetermined density along the axial direction at halfway between the first and second lattices. Furthermore, the improved FH curved boundary condition is also used for all the curved vessel walls.

In the simulation, in order to eliminate the instability of solutions, a converged solution for a relatively small value of Reynolds number is first used as the initial condition for a larger value of Reynolds number, and then the value of Reynolds number is increased gradually so that the converged solutions for the new larger values of Reynolds number can be obtained. Moreover, to improve the simulation precision and guarantee the flows next to the inlet and outlet to be fully developed, the inlet and outlet lengths of the simulated vessel should be increased and the lattices should be refined with larger Reynolds numbers. In actual computation, the length and node number are evaluated so that the velocity relative error between the simulated and analysed values on the cross sections near the inlet and outlet is kept at 2%.

4.2. Simulating results

4.2.1. Axial velocity

The development of the axial flow in the plane of symmetry for $y = 21.5$ as in Fig.6 (the abscissa of the bend centre) is shown in Fig.7. Velocity measurements are performed at seven axial stations in the bend: $\theta = 0°$, $30°$, $60°$, $90°$, $120°$, $150°$, and $180°$ along curved axis of the bent tube of the projection, and $\theta = 0°$ is the inlet and $\theta = 180°$ is the outlet of the curved tube.

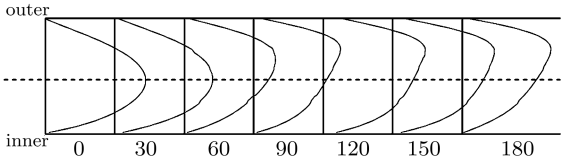


Fig.7. Development of the axial flow in the yz plane of symmetry; Re = 500.

In the velocity profiles at $\theta = 0°$ and 30°, the influence of the curvature is hardly visible and the parabolic velocity profile persists. Further along the downstream the maximum of axial velocity has shifted towards the outer bend, and at $\theta = 90°$ the shift reaches its maximum. A region of relatively low axial velocity appears near the inner bend, where the separation zones of the flow may exist with the increase of Re. Then the maximum of axial velocity shifts tardily towards the tube centre. At $\theta = 120°$ this region has developed into a plateau, in which the axial velocity becomes slow toward the centre of the tube. But gradually the plateau disappears and at $\theta = 150°$ a local minimum in the axial velocity is present at the tube centre.

A more complete picture of the axial flow development in the tube bend is given in Fig.8, in which the flow fields in the half circular cross-section along the tube axis at $\theta = 0°$, 30°, 60°, 90°, 120°, 150°, and 180° are given by iso-velocity contours.

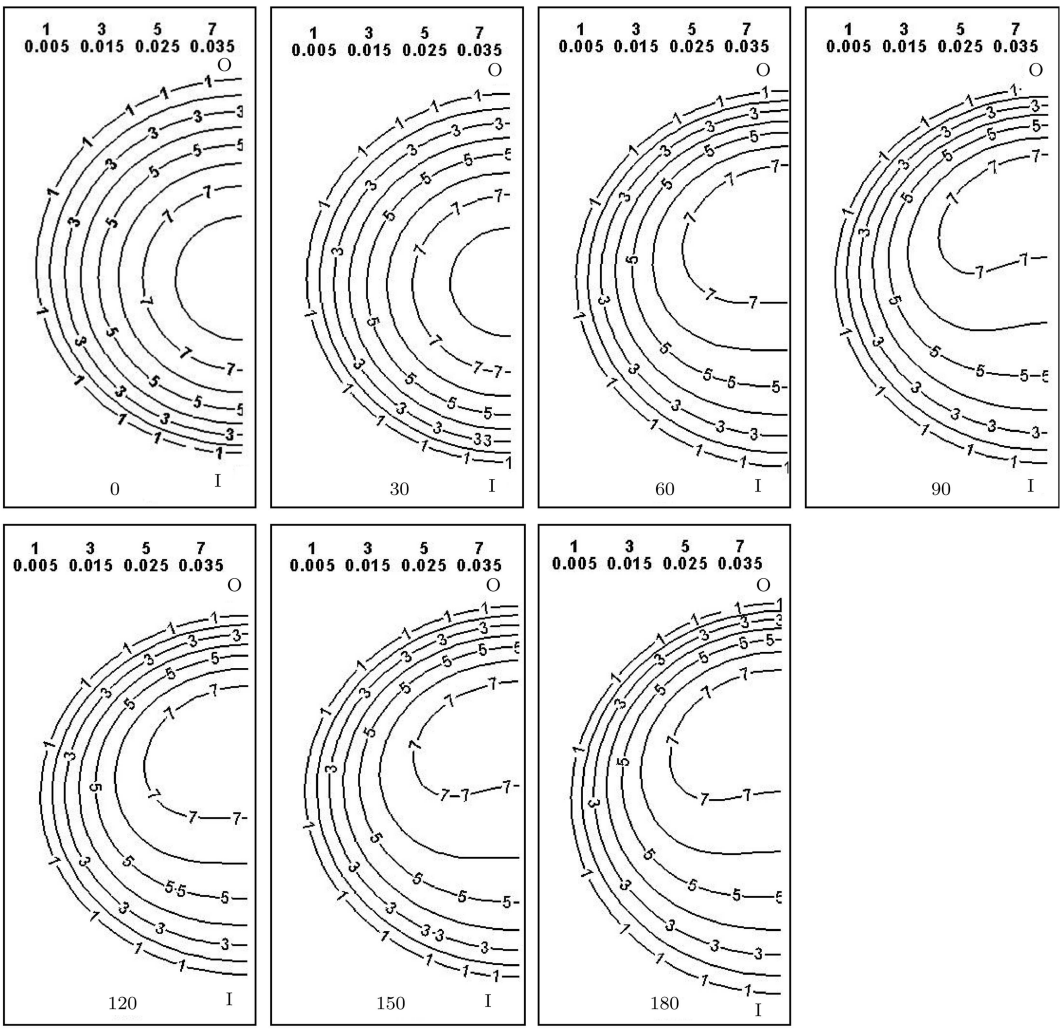


Fig.8. Development of axial flow represented by isovelocity contours at $\theta = 0°$, 300°, 60°, 90°, 120°, 150°, and 180° cross-sections respectively; Re = 500. (O: outer bend; I: inner bend.)

4.2.2. Secondary velocities

In Fig.9 the development of the secondary flow in the cross section of the bend at $\theta = 0°$, 30°, 60°, 90°, 120°, 150°, and 180° is shown respectively by vector plots.

At $\theta = 0°$, the secondary flow is completely directed from the outer towards the inner wall as a result of high pressure gradient near the outer wall of the bent tube. At $\theta = 5°$, the secondary flow moves from the inner wall to outer wall along the symmetric plane and the paired vortexes formed cover the whole cross-

section, where the fluid flows circumferentially back to the inner bend. The strength of the secondary flow increases gradually with the development of the flow, and the low-velocity fluid is carried to the inner wall side at $\theta = 30°$. At $\theta = 60°$, the secondary flow has its highest velocity. But near $\theta = 90°$, it is clearly that the strength of the secondary flow is conversely attenuated. Then, it increases a little at $\theta = 150°$. It should be pointed out that the strength of the secondary flow decreases rapidly in the downstream straight portion of the tube. Figure 9 also shows the secondary flows in the downstream straight tube part 48 lattice units away from the outlet of the bend, and the vortex that develops a 'tail'. With the increase of Re, the secondary flow enhances too.

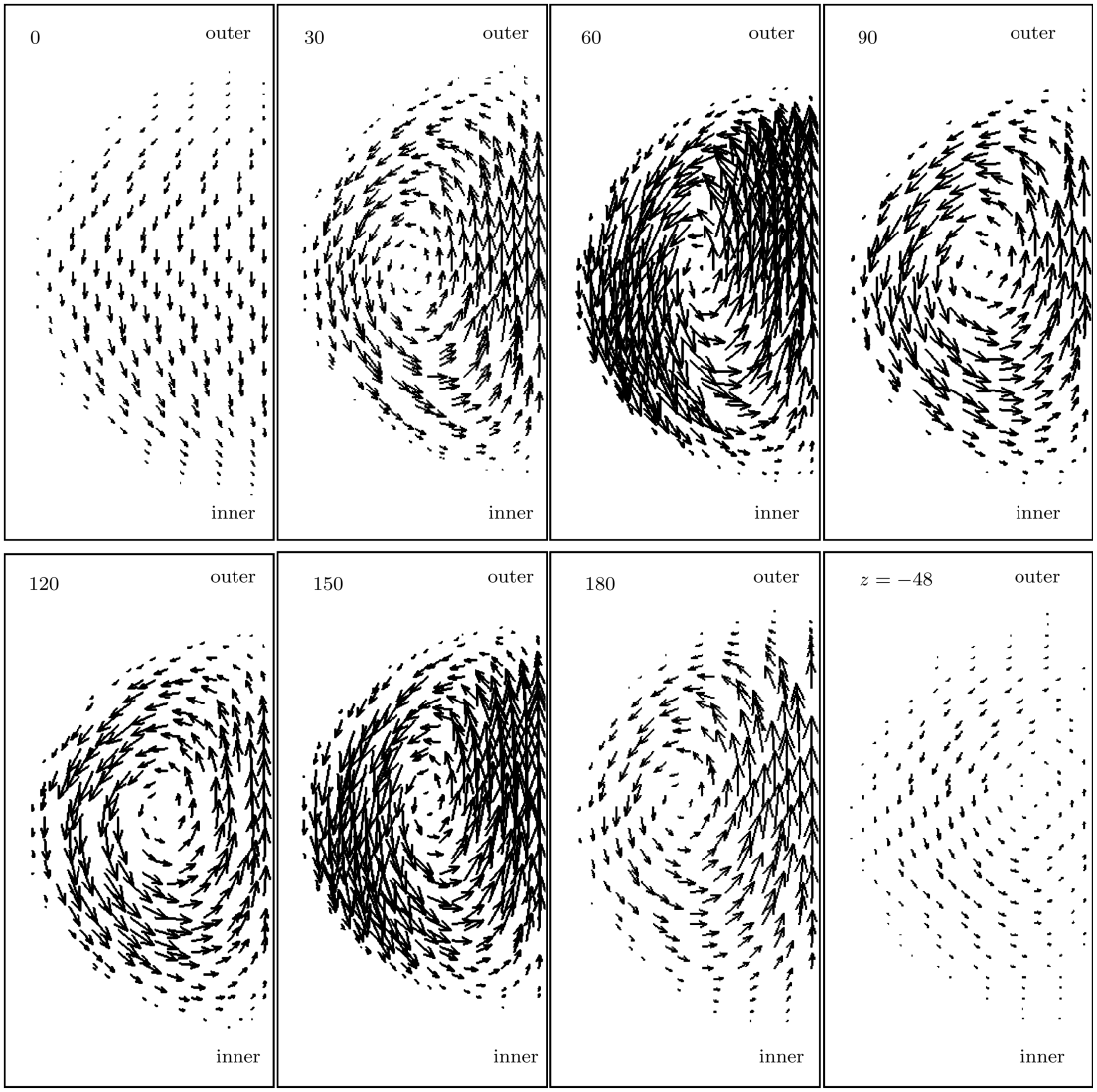


Fig.9. Development of secondary flow depicted in vector plots in the cross-sections of the bend; Re = 500.

4.2.3. Wall shear stress

Shear stress for a Newtonian fluid is usually estimated from gradients of measured or simulated velocity components, and the fluid viscosity. In many applications, especially in biological flows, the wall shear stress (WSS) plays a critical role. Early atherosclerotic lesions, for example, are thought to develop preferentially in arterial regions exposed to low and/or oscillatory WSS.

With the lattice Boltzmann model, the nine Cartesian components of local stress tensor are directly obtained using Eq.(7). The stress at any given point can be completely determined by this stress tensor. A real benefit of the lattice Boltzmann solver is

that these components are computed independently from the velocity gradients. Here, we compute and visualize the von Mises effective stress,[19] defined as

$$S_{\text{eff}} = \sqrt{\frac{A + 6B}{2}}, \tag{9}$$

where

$$A = (s_{xx} - s_{yy})^2 + (s_{yy} - s_{zz})^2 + (s_{zz} - s_{xx})^2, \tag{10}$$

$$B = s_{xy}^2 + s_{yz}^2 + s_{zx}^2. \tag{11}$$

The effective WSS distribution at the bend is presented in Fig.10. It should be noted that the flow along the inner wall of the entrance retains a high WSS. Also, along the outer wall, about one diameter in from the entrance, there is an area where the shear stress has a rather low value. This condition is caused by the tendency of the flow to take the shortest path along the inner wall. Near the exit of the pipe, in the area where the bend becomes straight section, another special interaction of the flows occurs, which tends to increase the wall shear along the outer wall and decrease it along the inner wall. This change in WSS can be simply explained by the continuation of the centrifugal tendency of the flow. The values of the wall shear at places away from the pipe entrance and at the exit agree quite well to those obtained by Hamakiotes and Berger.[20]

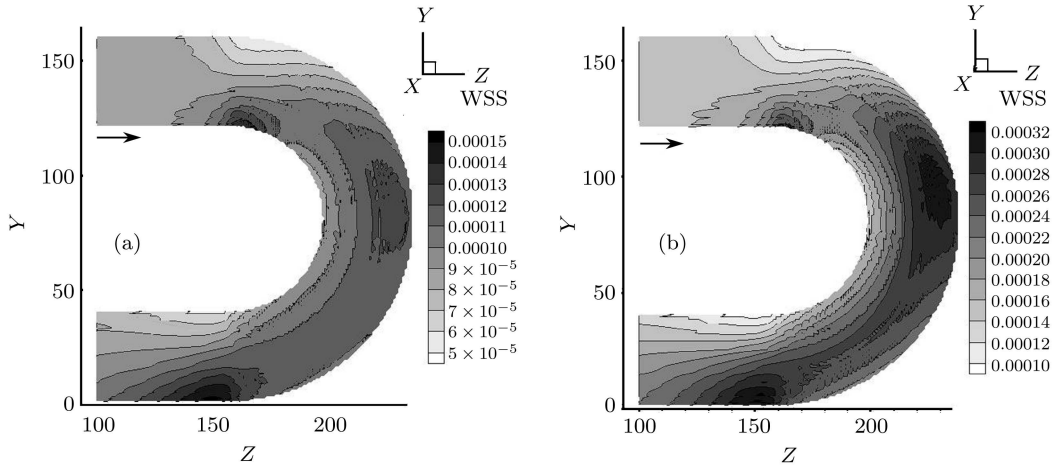


Fig.10. Effective shear stress distribution on the walls (WSS) of the bend; (a) Re = 500; (b) Re = 960.

As Re decreases and the flow decelerates, in a general sense, the WSS patterns are similar to each other except that the level of WSS is significantly lower. The entrance region of the flow is longer, and as the flow develops, there is a tendency for the wall shear to be higher along the outer wall relative to that along the inner wall. It should also be noted that the entrance region experiences quite low WSS as the flow adjusts itself to the pipe curvature.

5. Conclusions

In this paper we have addressed various issues related to 3D lattice Boltzmann method which are important in a practical point of view. We first discussed the effects of the bounce-back boundary condition, FH curved boundary condition, and the improved FH curved boundary condition under different Reynolds numbers for the 3DQ15 and 3DQ19 lattice Boltzmann models by simulating Poiseuille flow in a circular cylinder. The curved boundary conditions can give better results than the bounce-back boundary condition does, but the latter has much higher computational efficiency and system stability. Moreover, the 3DQ19 model is clearly superior to the 3DQ15 model in accuracy and stability.

In addition, we also study the dependence of computational error on the lattice resolution for 3DQ15, 3DQ19 and 3DQ27 lattice Boltzmann models. The 3DQ19 represents a good compromise in both computational efficient and reliability.

Besides the evaluation of the boundary conditions and the 3D lattice Boltzmann models, we have investigated the dependence of simulating error on the distribution of boundary relative to its local lattices. Although the computation error varies, the difference

in the error is limited in the same order of accuracy.

Finally, a numerical analysis has been performed for 3D aortic arch flow for different Reynolds numbers using the 3DQ19 lattice Boltzmann model with the improved FH curved boundary condition. Detailed description is given of the axial and secondary fluid velocities and the effective WSS in a 180° bend. The results show that a region of relatively low velocity and WSS appears near the inner wall of the bend, where the separation zones of the flow might exist with the increase of Re, and deposition of particular blood contents might occur and form arteriosclerosis. The results are also consistent with the previous studies by other methods, and are helpful for the understanding of the relationships among the arterial geometric complexity, arterial biomechanics, and arterial wall biology.

Acknowledgments

The authors would like to thank Professor Fang Hai-Ping for helpful discussion.

References

[1] Texon M 1963 *Role of Vascular Dynamics in the Development of Atherosclerosis* (New York: Academic) p167
[2] McDonald D A 1974 *Blood Flow in Arteries* vol 2 (London: Arnold) p432
[3] Qiu Y C and Tarbell J 2000 *J. Biomech. Eng.* **122** 77
[4] Dwyer H, Cheer A, Rutaganira T and Shacheraghi N 2001 *J. Fluids Eng.* **123** 869
[5] Sugiyama H and Hitomi D 2005 *Int. J. Numer. Mech. Fluids* **47** 1431
[6] Qian Y H, D'humiéres D and Lallemand P 1992 *Europhys. Lett.* **17** 479
[7] Kandhai D, Koponen A, Hoekstra A and Sloot P 1999 *J. Comput. Phys.* **150** 482
[8] Chen S Y, Chen H and Matinez D O 1991 *Phys. Rev. Lett.* **67** 3776
[9] Fang H P and Chen S Y 2004 *Chin. Phys.* **13** 47
[10] Liu M R and Kong L J 1996 *Acta Phys. Sin.* **45** 370 (in Chinese)
[11] Fang H P, Wang Z W, Lin Z F and Liu M R 2002 *Phys. Rev.* E **65** 051925
[12] Artoli A M, Kandhai D and Hoefsloot H C 2004 *J. Future Generation Computer Systems* **20** 909
[13] Boyd J, Buick J M, Cosgrove J A and Stansell P 2004 *Australas. Phys. Eng. Sci. Med.* **27** 207
[14] Li H B, Fang H P, Lin Z F, Xu S X and Chen S Y 2004 *Phys. Rev.* E **69** 031919
[15] Yu D Z, Mei R W and Luo L S 2003 *Progress in Aerospace Sciences* **39** 329
[16] Filippova O and Hanel D 1997 *Comput. Fluids* **26** 697
[17] Mei R W, Luo L S and Wei S 1999 *J. Comput. Phys.* **155** 307
[18] Zou Q S and He X Y 1997 *Phys. Fluids* **9** 1591
[19] Geiringer H 1953 *Advances in Applied Mechanics* III (New York: Academic) p200
[20] Hamakiotes C and Berger 1990 *J. Fluid Mech.* **210** 353